ADVANCED FUNCTIONAL MATERIALS
www.afm-journal.de

Synthesis of Hierarchically Porous Hydrogen Silsesquioxane Monoliths and Embedding of Metal Nanoparticles by On-Site Reduction

Nirmalya Moitra, Kazuyoshi Kanamori, Toyoshi Shimada, Kazuyuki Takeda, Yumi H. Ikuhara, Xiang Gao, and Kazuki Nakanishi**

A facile synthesis of a new class of reactive porous materials is reported: hierarchically porous hydrogen silsesquioxane ($HSiO_{1.5}$, HSQ) monoliths with well-defined macropores and mesopores. The HSQ monoliths are prepared via sol-gel accompanied by phase separation in a mild condition, and contain micrometer-sized co-continuous macropores and high specific surface area reaching up to 800 m^2 g^{-1} because of the small mesopores. A total preservation of Si–H, which is always an issue of HSQ materials, is confirmed by ^{29}Si solid-state NMR. The HSQ monolith has then been subjected to reduction of noble metal ions to their corresponding metal nanoparticles in simple aqueous solutions under an ambient condition. The nanoparticles produced in this manner are immobilized on the HSQ monolith and are characterized by X-ray diffraction (XRD) and high angle annular dark-field scanning transmission electron microscopy (HAADF-STEM). Both the bare HSQ and nanoparticles-embedded HSQ are promising as heterogeneous catalysts, exhibiting reusability and recyclability.

1. Introduction

Silsesquioxane ($RSiO_{1.5}$) materials consisting of random siloxane networks or polyhedral oligomeric silsesquioxane (POSS)-type cage structures have been attracting a great deal of attention from material chemists for many years, because of their wide applications in optics,[1] catalysis,[2] drug delivery,[3] and separation science.[4] The general synthetic route involves sol-gel technique applied to organoalkoxysilane precursors.[5] It can be synthesized in different forms such as particles,[6] monoliths,[7] and thin films.[8] After the discovery of template-directed synthesis of periodic mesoporous silicas (PMSs),[9] many bridged polysilsesquioxane materials containing periodic mesopores have been synthesized, which are called as periodic mesoporous organosilicas (PMOs).[6,10] Monolithic macroporous silsesquioxanes have also been synthesized by sol-gel accompanied by phase separation,[7,11] which is a reliable way to tailor tunable macropores in monoliths. In most cases, the reported polysilsesquioxane materials are bridged polysilsesquioxanes because these are easily synthesized from polysilylated organic precursors (bridged alkoxysilanes), and those prepared from organotrialkoxysilanes are relatively uncommon. Since the sol-gel process of simple organotrialkoxysilanes containing bulky organic moiety often suffers from the formation of segregated low-molecular-weight oligomers or polymers, uniform gelation based on the random network formation is hampered.[5a,12] In this context, we and Dong et al. have reported that macroporous monolithic methylsilsesquioxane (MSQ) can be synthesized using the phase separation-assisted sol-gel process directly from the molecular precursor, methyltrimethoxysilane (MTMS).[4c,7,11,13]

Another contending material in this category is hydrogen silsesquioxanes (HSQ, $HSiO_{1.5}$), or sometimes termed as hydridosilica or hydridosilsesquioxane, due to the presence of less bulky hydrogen attached to silicon. However, in spite of the comparable bond dissociation energies, the reactivity of Si–H in aqueous media is higher than Si–C probably due to the orbital overlap,[14] which makes it more vulnerable toward hydrolysis during the sol-gel process using the molecular precursors such as trialkoxysilane ($HSi(OR)_3$).[15] Under basic and/or nucleophilic conditions, attack of anion/nucleophile on the silicon of HSQ or trialkoxysilane precursor results in total or partial cleavage of Si–H moiety. This restricts the sol-gel route for HSQ to neutral of weakly acidic paths. Thus, only a few sol-gel-derived HSQ products have been reported in the form of film.[16] Recently, the group of Ozin has made a considerable progress for the preparation of periodically mesoporous particles from triethoxysilane.[17] However, to the best of our

Dr. N. Moitra, Dr. K. Kanamori, Dr. K. Takeda,
Prof. K. Nakanishi
Department of Chemistry
Graduate School of Science
Kyoto University
Kitashirakawa, Sakyo-ku, Kyoto 606-8502, Japan
E-mail: kanamori@kuchem.kyoto-u.ac.jp;
kazuki@kuchem.kyoto-u.ac.jp
Prof. T. Shimada
Department of Chemical Engineering
Nara National College of Technology
22 Yata-cho, Yamatokoriyama, Nara 639-1080, Japan
Dr. Y. H. Ikuhara, Dr. X. Gao
Nanostructures Research Laboratory
Japan Fine Ceramics Center
2-4-1 Mutsuno, Atsuta-ku, Nagoya 456-8587, Japan

DOI: 10.1002/adfm.201202558

knowledge, no monolithic materials with regulated porosity have been reported in spite of the advantage in building contact devices including, for example, catalytic reaction-separation devices. The high reactivity of trialkoxysilane precursors and the probability of Si–H decomposition during the sol-gel process are two major challenges that need to be overcome to synthesize HSQ macroporous monolith.

The usefulness of HSQ materials actually lies in the reactivity of Si–H bonds. Although the reduction behavior of Si–H moiety had long been confirmed, their activity and utility as the reactive sites on porous materials remained unexplored for many years. Brook and co-workers found that reduction of Karstedt's catalyst occurs on the Si–H-modified silica surfaces to give platinum nanoparticles which are active toward hydrosilylation.[18] Ozin and coworkers more recently reported the formation of silver nanoparticles in mesoporous HSQ microspheres by the reduction of silver(I) salt by a host-guest redox process.[19] In addition, Yanishpolskii et al. reported the formation of palladium nanoparticles on silane modified silica surface by the reduction of $Pd(NO_3)_2$.[20] These results demonstrate the activity of Si–H moiety for reduction of noble metal salts.

Herein, we present for the first time the synthesis of hierarchically porous HSQ monolith directly from a molecular precursor, trimethoxysilane (HTMS), by using sol-gel technique accompanied by phase separation processed under an ambient condition. The obtained monoliths retain well-defined micron-sized macropores and nanometer-sized mesopores with high surface area of ≈800 m^2 g^{-1} integrated in a hierarchical manner. A reasonable control of hydrolysis-polycondensation kinetics of HTMS and the preservation of the Si–H moiety in the final material is demonstrated. In addition, the reduction behavior by the Si–H moiety is exploited with noble metal salts ($AgNO_3$, $HAuCl_4$, $Pd(NO_3)_2$ and H_2PtCl_6) to corresponding metal nanoparticles. The redox chemistry between HSQ and metal salts and the size dependence of the metal nanoparticles are discussed.

2. Results and Discussion

2.1. Macropore Formation in HSQ Monoliths

The synthesis of HSQ monolith was performed under an acidic condition for catalyzing the hydrolysis-polycondensation of HTMS and to minimize the simultaneous hydrolysis of delicate Si–H bonds. The reaction of HTMS with 50 mM HNO_3 at room temperature results in the immediate formation of opaque precipitates. This is due to a high rate of hydrolysis and polycondensation of HTMS and to the occurrence of inhomogeneous segregation. Addition of solvent like methanol to the reaction mixture is one of the methods to adequately control the hydrolysis and condensation rates. Formation of monolithic gel was observed when methanol is used in the sol-gel reaction mixture containing HTMS. An increase in gelation time was observed with increasing amount of methanol. The gelation time of 15 min was obtained by mixing 2.5 mL of 50 mM HNO_3 and MeOH for hydrolysis of 2.1 mL (16.5 mmol) of HTMS. As concentration of acid and methanol amount in the reaction mixture influence the gelation time, the molar ratio of these components were fixed for convenience, HTMS:MeOH:H_2O:HNO_3: = 1:3.7:8.4:7.6 × 10^{-3}. See **Table 1** for detailed starting compositions.

Table 1. Starting compositions for monoliths preparation with different amounts of PEO.

Sample name	HTMS [mL]	PEO (M_n = 35000) [mg]	50 mM HNO_3 [mL]	MeOH [mL]
HY0	2.1	0	2.5	2.5
HY90	2.1	90	2.5	2.5
HY120	2.1	120	2.5	2.5
HY150	2.1	150	2.5	2.5
HY210	2.1	210	2.5	2.5
HY260	2.1	260	2.5	2.5

The gels produced in this manner were transparent and contained no obvious macropores (denoted as "nanoporous structure") (**Figure 1**a). The sol-gel process accompanied by phase separation is one of the most important methods for the facile formation of macropores and we have used this technique here. The phase separation inducer we have used for our system is poly(ethylene oxide) (PEO) with number average molecular weight of 35 000 Da, and increasing amount of PEO in the sol-gel reaction mixture results in a decrease in transparency in the resulting gels, indicating the macroporous structure is induced by phase separation. This can be verified from the scanning electron microscopy (SEM) images of the dried gels as shown in Figure 1a–e prepared by using increasing amount of PEO (Table 1). The increasing PEO changes the phase separation tendency to induce the morphological transformations from "nanoporous" to "particle aggregates" and then to "co-continuous". These changes of morphology in the gels are similar to the silica-PEO system as reported previously.[21] Therefore, the mechanism for phase separation should be analogous to the silica-PEO system and can be described by the adsorption of PEO on alkoxy-derived condensates, forming HSQ-PEO complexes by hydrogen bonding between silanol and ether oxygens of PEO. These complexes render the condensates more hydrophobic, which cause phase separation from the polar solvent by increasing enthalpic repulsive interaction. The silica-like phase separation tendency governed by hydrogen bonding in aqueous media in the present study agrees with that observed in the mesoporous HSQ formation driven by hydrogen bonding interaction with poly(ethylene oxide)-*block*-poly(propylene oxide)-*block*-poly(ethylene oxide) surfactant.[17] The phase separation tendency shows a maximum with a relatively small amount of PEO, and the tendency lowers with increasing PEO because of the weaker enthalpic repulsion between HSQ-PEO and the solvent phase containing excess PEO. At optimum amounts of PEO, the phase-separated structure shows co-continuous structure with well-defined macropores. Samples HY150 and HY210 show the co-continuous macroporous structure (Figure 1c,d, respectively) in the materials. An increasing amount of PEO from HY210 to HY260 in the reaction mixture leads to nanoporous structure without distinct macropores because phase separation tendency is lower. Indeed, a transparent gel-like HY0 was obtained in the case of HY260.

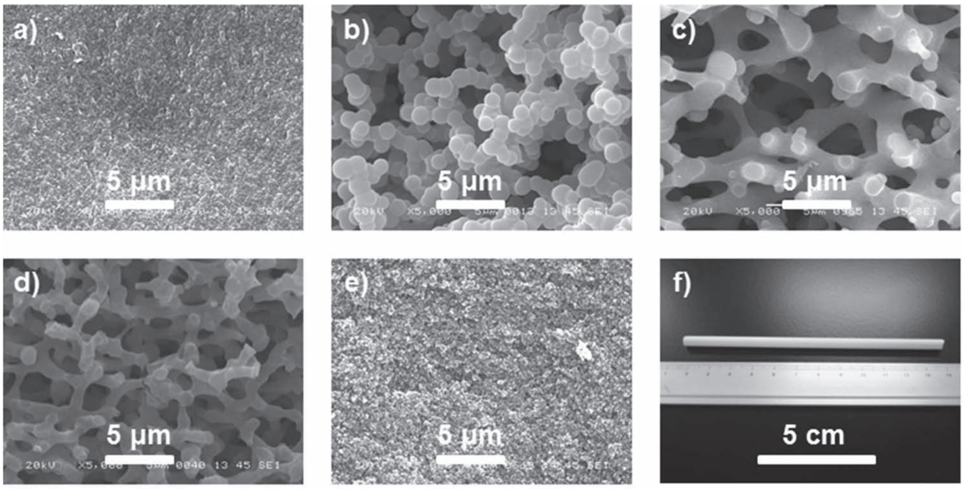

Figure 1. Scanning electron micrographs of dried HSQ monoliths prepared with different amounts of PEO, showing the varied phase-separating behavior. Changes in the gel morphology can be observed from a) HY0 nanoporous, to b) HY90 particle agreegate, c) HY150, and d) HY210 macroporous co-continuous structure, and then to e) HY280 nanoporous. f) Typical appearance of a column-shaped HY210 monolith.

The detailed characterization of macropores present in these samples was carried out by mercury porosimetry (**Figure 2**). The cumulative pore volume curves of HY150 and HY210 display the dependence of pore size and pore volume on the amount of PEO. An increase in the amount of PEO from HY150 to HY210 results in the decrease in macropore size but increase in pore volume. Moreover, the macropore size distribution curves show sharp distributions in the macropore region. In the case of HY150 and HY210, the peak pore diameters are 3.3 and 1.2 µm, respectively.

The presence of meso- and micropores in the material was revealed by nitrogen adsorption-desorption measurements (**Figure 3**). The adsorption–desorption isotherms of HY150 and HY210 show hysteresis of type IV,[22] evidencing the presence of mesopores in the material. In addition, high BET surface areas are observed for both HY150 (630 m^2 g^{-1}) and HY210 (800 m^2 g^{-1}) predominantly because of the small mesopores less than 10 nm as shown by the BJH pore size distribution curves obtained using adsorption branch (inset). The most dominant mesopore diameter of 3.2 nm is observed for HY210 which is decreased to ≈2 nm in the case of HY150.

2.2. Spectroscopic and Thermal Studies

Spectroscopic characterizations such as Fourier transform-IR (FT-IR), Raman and ^{29}Si solid-state cross-polarization/magic angle spinning (CP/MAS) NMR of HY210 were carried out to assess the molecular-level structure and preservation of Si–H bonds. The FT-IR (**Figure 4**(a)) and Raman (Figure S1) spectra of HY210 show a sharp Si–H stretching vibration at 2250 cm^{-1}. It also displays a strong Si–O–Si vibration at 1000–1250 cm^{-1} and O–Si–H vibration at 800–925 cm^{-1} in FT-IR. Since the absorption by Si-OH at around 930 cm^{-1} is negligible, a high crosslinking density and a complete preservation of Si–H in the siloxane-based network are suggested. The small amount of remaining phase separation inducer (PEO) in the resulting gel is observed by the broad peak of ether oxygen at around 1750 cm^{-1}. Further insight in the skeletal structure of HSQ monolith can be realized by carefully observing the peaks of FT-IR spectrum. The Si–O–Si and H–Si–O vibrations appearing at 1150 and 875 cm^{-1} are attributed to the cyclic structure whereas Si–O–Si and H–Si–O vibrations at 1070 and 830 cm^{-1} correspond to the random networks of HSQ.[23] Therefore, from the FT-IR

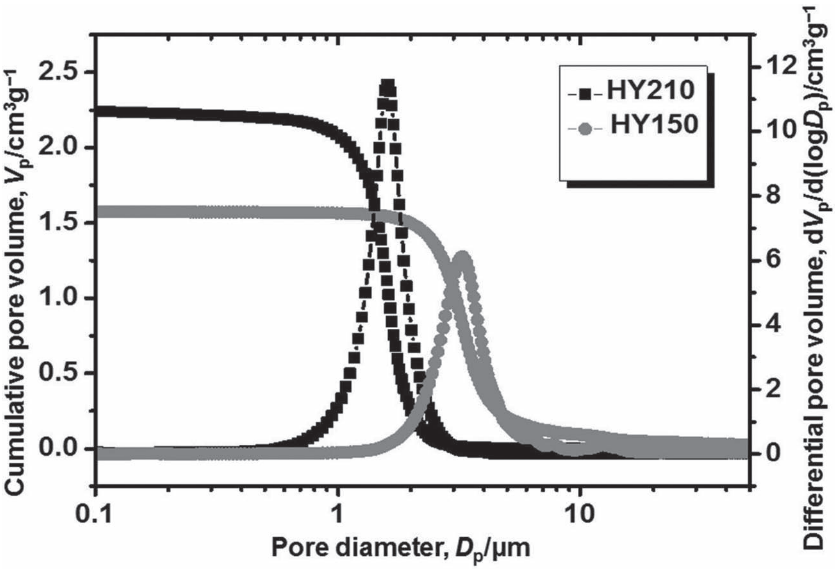

Figure 2. Pore size distributions of HSQ monoliths prepared with different amounts of PEO (HY150 and HY210). Increase in macropore size can be observed with a decrease in PEO content.

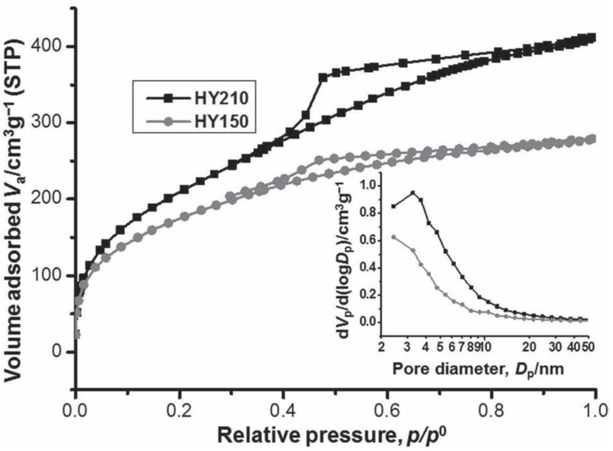

Figure 3. Nitrogen adsorption-desorption isotherms and BJH mesopore size distributions (inset) of HSQ monoliths (HY150 and HY210), showing the presence of small mesopores.

spectrum it can be concluded that the skeletons of HY210 monolith mainly consist of random networks and cyclic structures with preserved Si–H groups. In order to examine the thermal stability of HSQ monolith, thermogravimetry-differential thermal analysis (TG-DTA) of HY210 was performed (Figure 4b) under air with a heating rate of 5 °C min^{-1}. The TG and DTA curves show a major weight loss from 150 to 200 °C and a weight gain from 350 to 500 °C. The weight loss mainly corresponds to the combustion of PEO present in the dried HSQ sample. The weight gain is attributed to the thermal oxidation of Si–H to Si–O–Si and Si–OH.[24] This thermal decomposition temperature of Si–H moiety in HY210 is comparable to the thermal behavior reported for HSQ xerogels reported previously.[16,17] It can be concluded from TG-DTA analysis that the Si–H moiety present in HY210 is stable up to 350 °C.

The quantitative investigation of Si–H moiety present in HY210 can be determined by ^{29}Si solid-state CP/MAS NMR (Figure 4c). The "T" signal appearing in the NMR spectrum corresponds to the Si species consisting of $HSiX_3$ (X corresponds to OSi, OCH_3 or OH) units.[25] If hydrolysis of Si–H occurs, the "Q" species appear because of the SiX_4 units. In the spectrum, the T^3 peak is much larger than T^2 (94.5% T^3 vs 5.5% T^2 by peak areas) which indicates a high degree of condensation of HTMS in HY210. In addition, any Q signals are not observed, evidencing the complete preservation of Si–H in

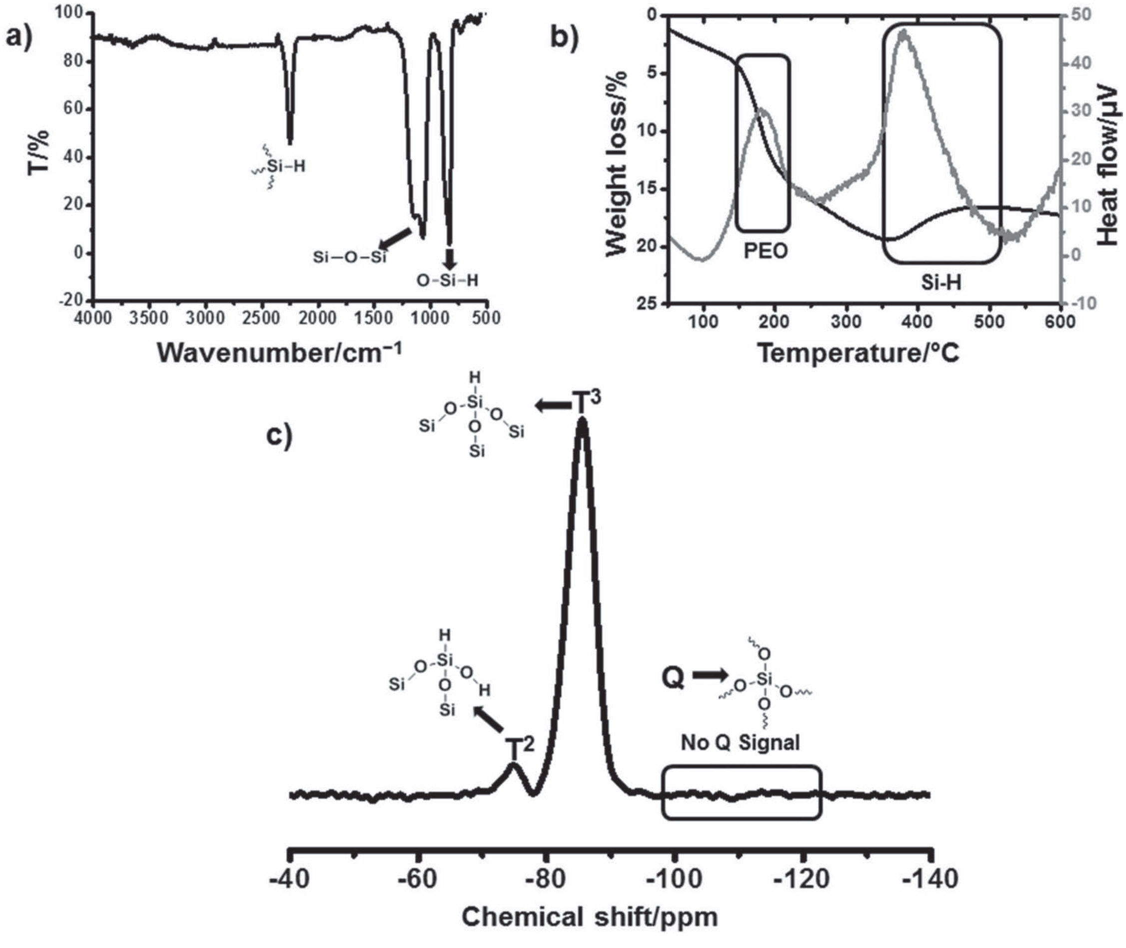

Figure 4. Spectroscopic and thermal characterizations of HSQ monolith HY210; a) FT-IR spectrum showing the appearance of Si–H (2250 cm^{-1}), Si–O–Si (1000–1250 cm^{-1}) and O-Si–H (800–925 cm^{-1}) vibrations, b) TG-DTA curve of HSQ showing the combustion of PEO (150–200 °C) and thermal oxidation of HSQ (360–500 °C), and c) ^{29}Si solid-state CP/MAS NMR revealing high condensation of HTMS and total preservation of Si–H bonds after the sol-gel process.

Table 2. Ratios of noble metal salts and dried HSQ monoliths reacted under aqueous ambient conditions.

Sample Name	HY210 [g]	0.1 M $AgNO_3$ [mL]
$Ag_{1/100}$	0.20	0.37
$Ag_{1/50}$	0.21	0.75
$Ag_{1/10}$	0.21	3.70
Sample Name	HY210 [g]	0.1 M $HAuCl_4$ [mL]
$Au_{1/100}$	0.19	0.37
$Au_{1/50}$	0.20	0.75
$Au_{1/10}$	0.21	3.70
Sample Name	HY210 [g]	0.1 M $Pd(NO_3)_2$ [mL]
$Pd_{1/100}$	0.20	0.37
$Pd_{1/50}$	0.21	0.75
$Pd_{1/10}$	0.20	3.70
Sample Name	HY210 [g]	0.1 M H_2PtCl_6 [mL]
$Pt_{1/100}$	0.20	0.37
$Pt_{1/50}$	0.20	0.75
$Pt_{1/10}$	0.21	3.70

HY210 presumably because of the use of limited amount of water compared to the previous study.[17] Therefore, according to ^{29}Si solid-state NMR of HY210, a total preservation of Si–H moiety in the material is confirmed in addition to the FT-IR and Raman results.

2.3. Redox Chemistry of HSQ Monoliths

These spectroscopic and thermal analyses of HY210 confirm the preservation and thermal stability of Si–H bonds. The Si–H bonds present in HSQ monolith are known to be stable toward hydrolysis under acidic and neutral aqueous conditions, and are active for reduction reactions. For example, reduction with monomers or polymethylhydrosiloxane (PMHS) containing Si–H is often used in organic synthesis.[26] In order to validate the redox property of HSQ monolith, HY210 was soaked in aqueous solutions containing noble metal salts with different concentrations as listed in **Table 2**. This procedure was carried out under ambient conditions. The addition of noble metal salt solutions to HY210 results in an immediate formation of hydrogen gas and simultaneous color change in the monolith. The oxidation of Si–H to Si–OH or Si–O–Si species simultaneously occurs with the reduction of noble metal salt and hydrogen formation, as described in Equation 1.[19]

$$n\mathrm{O}_{1.5}\mathrm{Si}-\mathrm{H} + \mathrm{M}^{n+} + n\mathrm{H}_2\mathrm{O} \rightarrow n\mathrm{O}_{1.5}\mathrm{Si}-\mathrm{OH} + \mathrm{M}(0) + n/2\mathrm{H}_2 + n\mathrm{H}^+, \text{ where } \mathrm{M}^{n+} = \mathrm{Ag}^+,\ \mathrm{Pd}^{2+},\ \mathrm{Au}^{3+},\ \text{and } \mathrm{Pt}^{4+} \tag{1}$$

The formed nanoparticles may further catalyze the oxidation of Si–H to Si-OH.[27] According to Equation 1, the amount of Si–H remaining in the material is inversely proportional to the amount of metal salts reacted. This can be verified from the FT-IR spectra of HY210 after being treated with different amounts of $AgNO_3$ (**Figure 5**, see also Supporting Information Figure S2–4 for other metal species). As the amount of Ag^+ increases from $Ag_{1/100}$ to $Ag_{1/10}$, the intensity of Si–H and O–Si–H vibration bands becomes lower, indicating oxidation of Si–H to Si–O. It can also be described from the increase in intensity of Si–OH stretching vibration (3300–3700 and 950 cm^{-1}) from $Ag_{1/100}$ to $Ag_{1/10}$. As the concentration of Ag^+ increases, the intensity of the Si–OH vibration also increases accordingly, proving the oxidation of Si–H to Si–OH. Furthermore, a partial demolition of cage like structure in the resulting material was observed by the decrease in intensities of cyclic Si–O–Si 1150 and 875 cm^{-1} with increasing amount of Ag^+, which needs more detailed study to be clarified though. The XRD patterns of resulting monoliths after being treated with $AgNO_3$, $HAuCl_4$, $Pd(NO_3)_2$, and H_2PtCl_6 confirm the formation of pure corresponding noble metal particles by their characteristic Bragg diffraction peaks (**Figure 6**a). The intensity of diffraction peaks is proportional to the amount of noble metal salt used. As the amount of the noble metal salts increases, the intensity of the diffractions of the monolith also increases accordingly, indicating a higher loading of the particles with increasing amount of metal salts (Figure 6b, see also Supporting Information Figure S5–7 for other metal species).

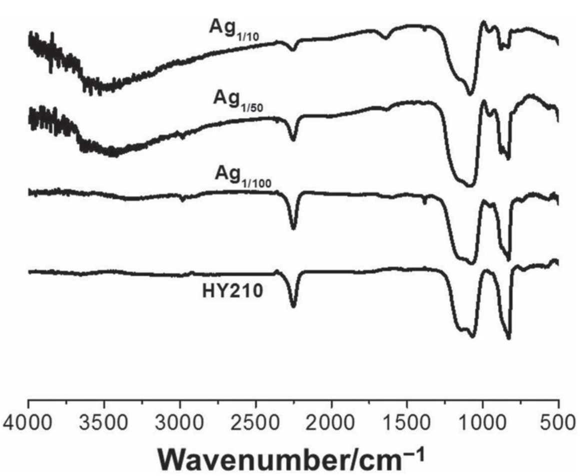

Figure 5. FT-IR spectra of HY210 after being treated with different amounts of $AgNO_3$. Decrease in Si–H and O-Si–H and increase in Si–OH vibrations can be observed with increasing amount of $AgNO_3$.

The metal particle sizes can be estimated from XRD by employing the Scherrer's equation.[28] The average size of all metal particles (Ag, Au, Pd, and Pt) produced in the monolith are in the range of nanometers (**Table 3**). The silver and gold nanoparticles formed in the monolith have the largest average particle size followed by palladium and then platinum. It is noteworthy that the average particle sizes calculated from the Scherrer's equation are not dependent on the concentration of the noble metal salt solution, but on the type of the metal. The standard electrode potential values (E^0 vs standard hydrogen electrode (SHE)) of the metal cations are directly related to the average size of nanoparticles, whereas the charge in the metal ions (oxidation number, *n*) is inversely related. Note that oxidation of Si–H to Si–O$^-$ in water occurs at −1.23 V,[29] which

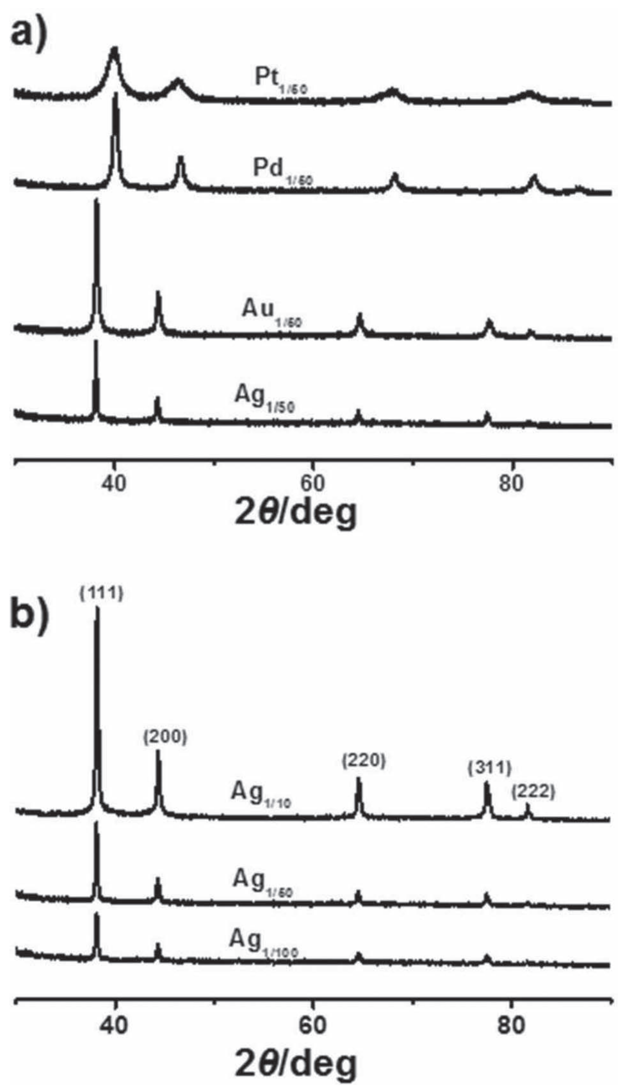

Figure 6. XRD patterns of HY210 after being treated with a) 1/50 equivalent of noble metal salts, showing the appearance of characteristic Bragg peaks of metal particles and b) different amounts of $AgNO_3$, showing increasing intensity with increasing amount of Ag^+.

is enough lower than the E^0 values of metal ions. This relation becomes clear when we compare the size of the metal nanoparticles with standard electrode potential and charge of the metal salts. As the ratio of E^0/n increases for any metal salt, the average size of nanoparticles also increases accordingly (**Figure 7**).

2.4. Characterization by HAADF-STEM

In order to analyze the microstructure of the nanoparticles produced in the monolith, HAADF-STEM was employed.[30] **Figure 8** shows the typical HAADF-STEM images of the monoliths with distributed metal nanoparticles (Ag, Au, Pd, and Pt). In HAADF-STEM, the image contrast is roughly proportional to the square of the atomic number Z.[31] Consequently, dispersed metal nanoparticles (Ag (Z = 47), Au (Z = 79), Pd (Z = 46) and Pt (Z = 78)) display brighter contrasts in the HSQ monoliths consisting of H (Z = 1), O (Z = 8) and Si (Z = 14) in Figure 8. The high resolution HAADF-STEM images reveal that the metal nanoparticles are not only located on the macropore skeletons, but also embedded inside the skeletons (inset). The metal salt solution diffused inside the skeletons through the mesopores, forming metal nanoparticles by being reduced there. The particles growth may be spatially restricted inside the skeletons, resulting in smaller particles compared to those on the macropore skeletons. In the case of $Ag_{1/10}$, $Au_{1/10}$, $Pd_{1/10}$ and $Pt_{1/10}$, a wide size range of particles was observed. For $Ag_{1/10}$, the particle size varied from 1 to 200 nm. Comparable result was obtained for $Au_{1/10}$ where the particle size ranged from 5 to 150 nm. However, an apparent decrease in the range of particle size was observed for both $Pd_{1/10}$ and $Pt_{1/10}$ where the particle size ranged from 5 to 50 nm and 1 to 50 nm, respectively. The observed size ranges agree well with the average sizes calculated by the Scherrer's equation as listed in Table 3.

After the reduction of metal salts, the dried monoliths did not have any cracks. The SEM images of the $Ag_{1/10}$, $Au_{1/10}$, $Pd_{1/10}$ and $Pt_{1/10}$ monoliths show the preservation of the co-continuous macroporous structure like original HY210 (Supporting Information Figure S8). These results demonstrate the high stability of macroporous structure in the HSQ monoliths toward reduction of noble metal salts.

While a small number of the metal nanoparticles are located on the macropore surface without a strong interaction, most of them are immobilized within the macropore skeletons of HSQ predominantly by physical confinement. Indeed, washing of the monolith with water, alcohol (methanol and ethanol), and hexane shows no indication of leaching. The HSQ monolith therefore acts not only as a reducing agent for noble metal salts but also as a host for produced nanoparticles after the reduction. The nitrogen adsorption-desorption measurements on $Ag_{1/100}$, $Ag_{1/50}$ and $Ag_{1/10}$ monoliths confirm the preservation of the high specific surface areas (Supporting Information Table S1). The adsorption-desorption isotherms of these treated monoliths also show type IV, revealing the presence of open mesopores as displayed in Supporting Information Figures S9,S10. A slight decrease of specific surface area is observed from $Ag_{1/100}$ to $Ag_{1/10}$. This can be ascribed to the partial blocking of meso- and micropores of HY210 by increasing amount of Ag nanoparticles.

The metal nanoparticle-supported porous monoliths can be further used as highly efficient heterogeneous catalysts for organic synthesis such as the Suzuki–Miyaura coupling and Mizoroki–Heck reaction, which we will report in the near future. Different from the fact that most metal nanoparticles are supported or stabilized by ligands such as hydroxyl, thiol and amino groups,[32] these nanoparticles formed on HSQ are supported with no ligands, which is advantageous to the catalytic activity of the nanoparticles.

3. Conclusions

Herein, we have successfully demonstrated the synthesis of hierarchically porous HSQ monoliths with well-defined macropores

Table 3. Comparison of metal particle sizes with standard electrode potential and oxidation state.

Sample Name	Standard electrode potential-oxidation number ratio, E^0n^{-1} [V]	Average particle size from XRD [nm]	Particle size range from HAADF-STEM [nm]
$Ag_{1/10}$	0.80	45.9	1-200
$Ag_{1/50}$	0.80	46.2	*N/A*
$Ag_{1/100}$	0.80	45.5	*N/A*
$Au_{1/10}$	0.51	36.1	5–150
$Au_{1/50}$	0.51	35.9	*N/A*
$Au_{1/100}$	0.51	36.0	*N/A*
$Pd_{1/10}$	0.46	22.6	5–50
$Pd_{1/50}$	0.46	22.7	*N/A*
$Pd_{1/100}$	0.46	21.5	*N/A*
$Pt_{1/10}$	0.18	6.3	1–50
$Pt_{1/50}$	0.18	6.7	*N/A*
$Pt_{1/10}$	0.18	6.9	*N/A*

by the sol-gel process accompanied by phase separation. The dependence of gel morphology on the concentration of phase separation inducer PEO is also discussed. Precise control of the macropore size in the material is achieved just by changing the amount of PEO within a particular range. A complete preservation of Si–H is revealed by spectroscopic characterizations such as ^{29}Si solid-state NMR. The FT-IR spectra show the molecular-level structures of HSQ monoliths, which reveals the presence of random network and cage structures. High thermal stability of Si–H bond is verified from the thermogravimetric analysis.

The reductive ability of this monolith has successfully been demonstrated by reduction of noble metal salts under ambient aqueous conditions. It is noteworthy that Si–H groups present inside the skeletons as well as on the macropore surfaces contribute to the reduction, which leads to the formation of corresponding metal nanoparticles not only on the macropore skeletons but also inside the skeletons. These nanoparticles have relatively broad size distributions. The particle sizes are also verified from HAADF-STEM images of the nanoparticle-embedded monoliths.

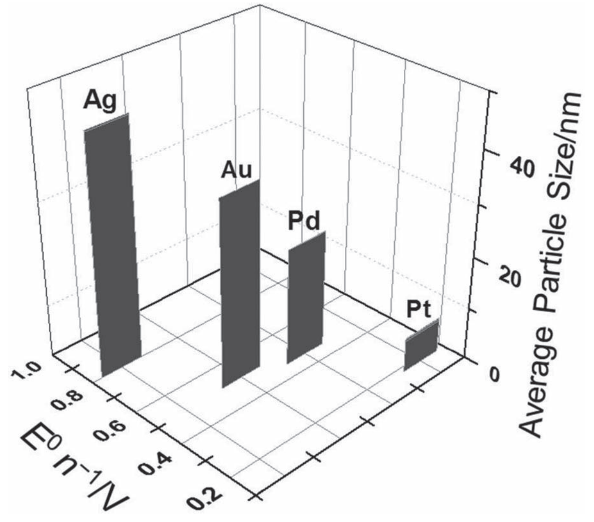

Figure 7. Decrease in average metal nanoparticle sizes calculated by using the Scherrer's equation with decrease in the ratio of standard electrode potential (E^0) and oxidation number (n) of metal salt.

These findings of host–guest redox chemistry on hierarchically porous HSQ monoliths will open a path for a new type of chemically-active monolithic macroporous materials, and both bare HSQ monoliths and nanoparticles-embedded monoliths would provide a highly efficient tool as the heterogeneous catalyst. The reaction between Si–H and metal precursors should be comprehensively explored in order to precisely control the size and shape of the nanoparticles. Our future report will explore the catalytic behavior of these materials. Furthermore, the possibility of formation of alloy metal nanoparticles by co-reduction of multiple metal precursors will also be investigated for applications such as to continuous flow reactors and separation media.[33]

4. Experimental Section

Materials: Trimethoxysilane (HTMS) (>90%, Tokyo Chemical Industry Co., Ltd. (Japan)), poly(ethylene oxide) with the number average molecular weight of 35 000 Da (PEO) (Sigma-Aldrich Co. LLC (USA)), methanol (MeOH) (Kishida Chemical Co., Ltd. (Japan)), nitric acid (65 wt%, Kishida Chemical Co., Ltd. (Japan)), distilled water (Hayashi Pure Chemical Industry, Ltd. (Japan)), silver nitrate (Sigma-Aldrich Co. LLC (USA)), chloroauric acid tetrahydrate (Kishida Chemical Co., Ltd. (Japan)), palladium nitrate (Wako Pure Chemical Industries, Ltd. (Japan)] and chloroplatinic acid hexahydrate (Tokyo Chemical Industry Co., Ltd. (Japan)) were used as received.

Characterization: The observation of microstructures of the fractured surfaces of the samples was conducted under a scanning electron microscope (SEM, JSM-6060S, JEOL Ltd. (Japan)). Macropores in the samples were characterized by using a mercury porosimeter (Pore Master 60-GT, Quantachrome Instruments (USA)). The meso- and micropores present in the sample were analyzed by nitrogen adsorption-desorption measurements (BELSORP-mini II, BEL Japan, Inc. (Japan)). The samples were degassed at 200 °C for 6 h before each measurement. The Fourier transform-IR (FT-IR) spectra of the samples were recorded on an FT-IR spectrometer (IRAffinity-1, Shimadzu Corp. (Japan)) using ground samples that were mixed with KBr, and Raman spectra were recorded using a confocal Raman spectrometer (Xplora, Horiba, Ltd. (Japan)).

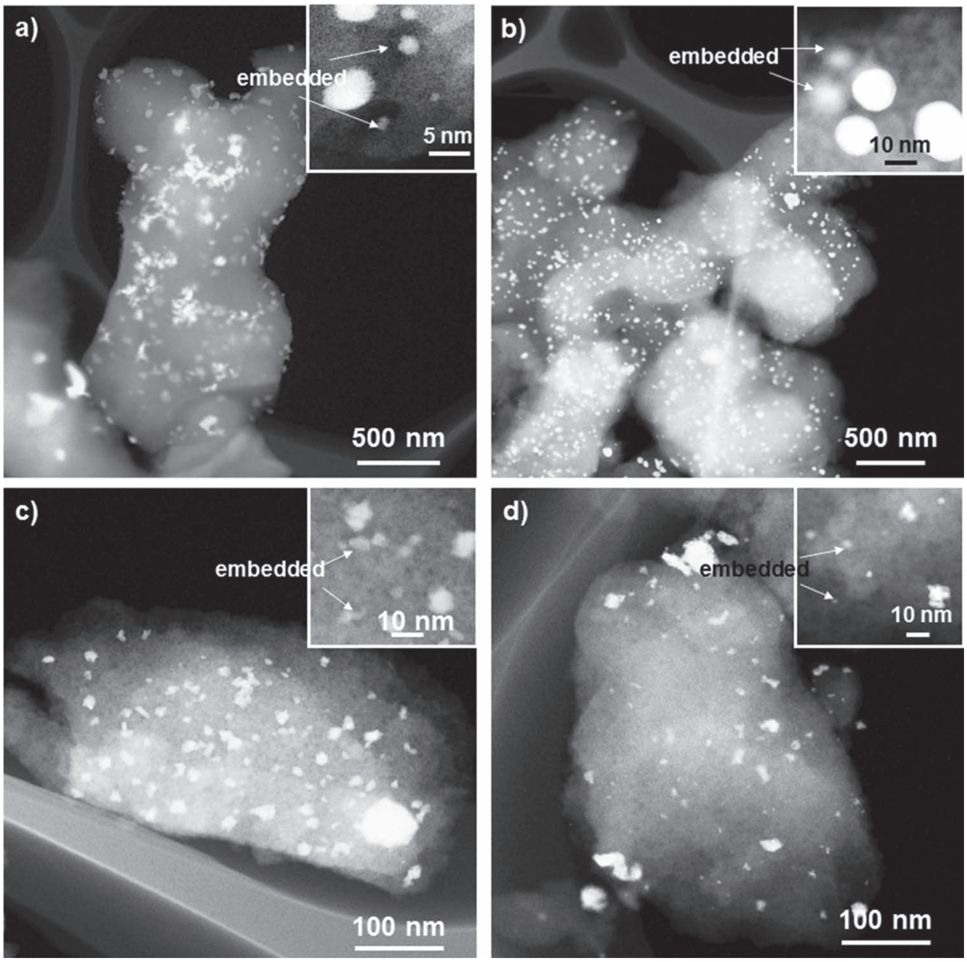

Figure 8. HAADF-STEM images of a) $Ag_{1/10}$ b) $Au_{1/10}$ c) $Pd_{1/10}$, and d) $Pt_{1/10}$, showing the immobilized nanoparticles on the macropore surface and formation of small nanoparticles inside the mesopores present in the material (inset).

Solid-state ^{29}Si cross-polarization/magic angle spinning (CP/MAS) NMR experiment was performed at room temperature in a magnetic field of 7 T on an OPENCORE NMR spectrometer[34] operating at 299.52 MHz (for ^1H) and 59.507 MHz (for ^{29}Si) using a 5-mm MAS probe. The sample spinning frequency was 5 kHz and the contact time was 10 ms. We found no appreciable change in the resonance-line shape between the spectra obtained by the CP and single-pulse techniques. Thermogravimetry-differential thermal analysis (TG-DTA) measurements were performed on Thermo Plus TG 8120 (Rigaku Corp. (Japan)) at a heating rate of 5 °C min^{-1} while continuously supplying air at 100 mL min^{-1}. The X-ray diffraction (XRD) of noble metal nanoparticles immobilized in the monoliths was recorded by a powder X-ray diffractometer (RINT Ultima III, Rigaku Corp. (Japan)) using Cu Kα (λ = 0.154 nm) as an incident beam. To characterize the size of the nanoparticles and their spatial distribution within the monoliths, high angle annular dark-field scanning transmission electron microscopy (HAADF-STEM) was employed. The obtained composite samples were crushed into powders and then deposited on micro-grids covered by carbon films for HAADF-STEM observation. The high-resolution TEM observations were performed using a 200 kV JEM-2100F (JEOL Ltd. (Japan)) microscope with an STEM unit equipped with a spherical-aberration corrector (CEOS GmbH (Germany)), which provides a minimum probe of about 0.1 nm in diameter. During HAADF-STEM imaging, a probe convergence angle of 25 mrad and an annular dark-field detector with an inner angle greater than 52 mrad were used.

Synthesis of Hydrogen Silsesquioxane Monolith: In a typical synthetic procedure, a given amount of PEO (Table 1) was dissolved in 1:1 (in volume) mixture of 50 mM HNO_3 aq. (2.5 mL) and methanol (2.5 mL). This mixture was stirred at room temperature for 30 min. To this solution HTMS (2.1 mL) was added. This mixture was stirred for 2 min, and then the stirring was stopped and left at room temperature. Gelation occurs within 15 min. This gel was aged at room temperature for 2 days, followed by washing with methanol and then it was dried at 40 °C for 2 days.

Noble Metal Nanoparticle Formations: A piece of HY210 (≈0.20 g, ≈3.8 mmol) was soaked in 20 mL of distilled water and left at room temperature for 3 h for water to diffuse through the macropores. A given amount of metal salt solution was then added as described in Table 2, and the whole mixture was left at room temperature for 3 h. Change in color of monolith and hydrogen evolution were immediately observed. After 3 h, the hydrogen evolution was stopped. The supernatant solution was decanted and monolith was washed 3 times with methanol (20 mL). This monolith was dried under air for 2 days at 40 °C. Each sample name denotes the kind of metal followed by metal/HY210 molar ratio.

Supporting Information

Supporting Information is available from the Wiley Online Library or from the author.

Acknowledgements

The present work was financially supported by the Advanced Low Carbon Technology Research and Development Program (ALCA) from the Japan Science and Technology Agency (JST). Prof. Yuichi Ikuhara (Tokyo University) is acknowledged for HAADF-STEM observations of nanoparticles-embedded HSQ monoliths.

Received: September 6, 2012
Published online: December 27, 2012

[1] a) C. Sanchez, B. Lebeau, F. Chaput, J.-P. Boilot, *Adv. Mater.* **2003**, *15*, 1969–1994; b) D. P. Fasce, R. J. J. Williams, L. Matejka, J. Plestil, J. Brus, B. Serrano, J. C. Cabanelas, J. Baselga, *Macromolecules* **2006**, *39*, 3794–3801; c) D. J. Sirbuly, S. E. Létant, T. V. Ratto, *Adv. Mater.* **2008**, *20*, 4724–4727; d) S. Inagaki, O. Ohtani, Y. Goto, K. Okamoto, M. Ikai, K. Yamanaka, T. Tani, T. Okada, *Angew. Chem. Int. Ed.* **2009**, *48*, 4042–4046; e) J. Graffion, X. Cattoën, M. Wong Chi Man, V. R. Fernandes, P. S. Andre, R. A. S. Ferreira, L. D. Carlos, *Chem. Mater.* **2011**, *23*, 4773–4782; f) J. Graffion, X. Cattoën, V. T. Freitas, R. A. S. Ferreira, M. Wong Chi Man, L. D. Carlos, *J. Mater. Chem.* **2012**, *22*, 6711–6715.

[2] a) H. C. L. Abbenhuis, *Chem. Eur. J.* **2000**, *6*, 25–32; b) K. Wada, N. Itayama, N. Watanabe, M. Bundo, T. Kondo, T. A. Mitsudo, *Organometallics* **2004**, *23*, 5824–5832; c) A. Brethon, C. Bied, J. J. E. Moreau, M. Wong Chi Man, *J. Sol-Gel Sci. Technol.* **2009**, *50*, 141–151; d) E. A. Quadrelli, J.-M. Basset, *Coord. Chem. Rev.* **2010**, *254*, 707–728; e) S. Sakugawa, K. Wada, M. Inoue, *J. Catal.* **2010**, *275*, 280–287; f) A. Monge-Marcet, R. Pleixats, X. Cattoën, M. Wong Chi Man, *Catal. Sci. Technol.* **2011**, *1*, 1544–1563.

[3] a) C. McCusker, J. B. Carroll, V. M. Rotello, *Chem. Commun.* **2005**, 996–998; b) T. L. Kaneshiro, X. Wang, Z.-R. Lu, *Mol. Pharmaceutics* **2007**, *4*, 759–768; c) H. Ghanbari, B. G. Cousins, A. M. Seifalian, *Macromol. Rapid Commun.* **2011**, *32*, 1032–1046.

[4] a) K. D. Wyndham, J. E. O'Gara, T. H. Walter, K. H. Glose, N. L. Lawrence, B. A. Alden, G. S. Izzo, C. J. Hudalla, P. C. Iraneta, *Anal. Chem.* **2003**, *75*, 6781–6788; b) J. S. Mellors, J. W. Jorgenson, *Anal. Chem.* **2004**, *76*, 5441–5450; c) K. Kanamori, H. Yonezawa, K. Nakanishi, K. Hirao, H. Jinnai, *J. Sep. Sci.* **2004**, *27*, 874–886; d) M. Wu, R. Wu, R. Li, H. Qin, J. Dong, Z. Zhang, H. Zou, *Anal. Chem.* **2010**, *82*, 5447–5454.

[5] a) D. A. Loy, B. M. Baugher, C. R. Baugher, D. A. Schneider, K. Rahimian, *Chem. Mater.* **2000**, *12*, 3624–3632; b) K. J. Shea, D. A. Loy, *Acc. Chem. Res.* **2001**, *34*, 707–716.

[6] N. Mizoshita, T. Tani, S. Inagaki, *Chem. Soc. Rev.* **2011**, *40*, 789–800.

[7] K. Kanamori, K. Nakanishi, *Chem. Soc. Rev.* **2011**, *40*, 754–770.

[8] L. Nicole, C. Boissière, D. Grosso, A. Quach, C. Sanchez, *J. Mater. Chem.* **2005**, *15*, 3787–3811.

[9] C. T. Kresge, M. E. Leonowicz, W. J. Roth, J. C. Vartuli, J. S. Beck, *Nature* **1992**, *359*, 710–712.

[10] a) T. Asefa, M. J. MacLachlan, N. Coombs, G. A. Ozin, *Nature* **1999**, *402*, 867–871; b) Y. Lu, H. Fan, N. Doke, D. A. Loy, R. A. Assink, D. A. LaVan, C. J. Brinker, *J. Am. Chem. Soc.* **2000**, *122*, 5258–5261; c) S. Inagaki, S. Guan, T. Ohsuna, O. Terasaki, *Nature* **2002**, *416*, 304–307.

[11] a) K. Nakanishi, K. Kanamori, *J. Mater. Chem.* **2005**, *15*, 3776–3786; b) K. Nakanishi, N. Tanaka, *Acc. Chem. Res.* **2007**, *40*, 863–873.

[12] a) L. Matějka, O. Dukh, D. Hlavatá, B. Meissner, J. Brus, *Macromolecules* **2001**, *34*, 6904–6914; b) H. Dong, M. Lee, R. D. Thomas, Z. Zhang, R. F. Reidy, D. W. Mueller, *J. Sol-Gel Sci. Technol.* **2003**, *28*, 5–14; c) H. Dong, Z. Zhang, M.-H. Lee, D. W. Mueller, R. F. Reidy, *J. Sol-Gel Sci. Technol.* **2007**, *41*, 11–17.

[13] a) H. Dong, M. A. Brook, J. D. Brennan, *Chem. Mater.* **2005**, *17*, 2807–2816; b) H. J. Dong, J. D. Brennan, *Chem. Mater.* **2006**, *18*, 4176–4182; c) K. Kanamori, Y. Kodera, G. Hayase, K. Nakanishi, T. Hanada, *J. Colloid Interface Sci.* **2011**, *357*, 336–344.

[14] R. Walsh, *Acc. Chem. Res.* **1981**, *14*, 246–252.

[15] M. Pauthe, J. Phalippou, R. Corriu, D. Leclercq, A. Vioux, *J. Non-Cryst. Solids* **1989**, *113*, 21–30.

[16] a) K. Matsui, M. Tominaga, Y. Arai, H. Satoh, M. Kyoto, *J. Non-Cryst. Solids* **1994**, *169*, 295–300; b) Y.-S. Li, A. Ba, *Spectrochim. Acta, Part A* **2008**, *70*, 1013–1019; c) G. Das, L. Ferraioli, P. Bettotti, F. De Angelis, G. Mariotto, L. Pavesi, E. Di Fabrizio, G. D. Soraru, *Thin Solid Films* **2008**, *516*, 6804–6807.

[17] Z. Y. Xie, E. J. Henderson, O. Dag, O. W. Wang, J. E. Lofgreen, C. Kubel, T. Scherer, P. M. Brodersen, Z. Z. Gu, G. A. Ozin, *J. Am. Chem. Soc.* **2011**, *133*, 5094–5102.

[18] H. A. Ketelson, M. A. Brook, R. Pelton, Y. M. Heng, *Chem. Mater.* **1996**, *8*, 2195–2199.

[19] O. Dag, E. J. Henderson, W. Wang, J. E. Lofgreen, S. Petrov, P. M. Brodersen, G. A. Ozin, *J. Am. Chem. Soc.* **2011**, *133*, 17454–17462.

[20] N. Ivashchenko, V. Tertykh, V. Yanishpolskii, J. Skubiszewska-Zieba, R. Leboda, S. Khainakov, *J. Therm. Anal. Calorim.* **2012**, *108*, 1121–1127.

[21] a) K. Nakanishi, H. Komura, R. Takahashi, N. Soga, *Bull. Chem. Soc. Jpn.* **1994**, *67*, 1327–1335; b) K. Nakanishi, N. Soga, *Bull. Chem. Soc. Jpn.* **1997**, *70*, 587–592.

[22] K. S. W. Sing, D. H. Everett, R. A. W. Haul, L. Moscou, R. A. Pierotti, J. Rouquerol, T. Siemieniewska, *Pure Appl. Chem.* **1985**, *57*, 603–619.

[23] a) C. L. Frye, W. T. Collins, *J. Am. Chem. Soc.* **1970**, *92*, 5586–5588; b) P. Bornhauser, G. Calzaferri, *J. Phys. Chem.* **1996**, *100*, 2035–2044; c) E. S. Park, H. W. Ro, C. V. Nguyen, R. L. Jaffe, D. Y. Yoon, *Chem. Mater.* **2008**, *20*, 1548–1554; d) E. J. Henderson, J. A. Kelly, J. G. C. Veinot, *Chem. Mater.* **2009**, *21*, 5426–5434.

[24] a) V. Belot, R. Corriu, D. Leclercq, P. H. Mutin, A. Vioux, *Chem. Mater.* **1991**, *3*, 127–131; b) V. Belot, R. J. P. Corriu, D. Leclercq, P. H. Mutin, A. Vioux, *J. Polym. Sci., Part A: Polym. Chem.* **1992**, *30*, 613–623; c) R. J. P. Corriu, D. Leclercq, *Angew. Chem. Int. Ed.* **1996**, *35*, 1420–1436.

[25] G. D. Sorarù, G. D'Andrea, R. Campostrini, F. Babonneau, *J. Mater. Chem.* **1995**, *5*, 1363–1674.

[26] a) H. Mimoun, J. Y. de Saint Laumer, L. Giannini, R. Scopelliti, C. Floriani, *J. Am. Chem. Soc.* **1999**, *121*, 6158–6166; b) N. J. Lawrence, S. M. Bushell, *Tetrahedron Lett.* **2000**, *41*, 4507–4512; c) Y. Motoyama, K. Mitsui, T. Ishida, H. Nagashima, *J. Am. Chem. Soc.* **2005**, *127*, 13150–13151; d) A. C. Fernandes, C. C. Romão, *Tetrahedron* **2006**, *62*, 9650–9654.

[27] T. Mitsudome, A. Noujima, T. Mizugaki, K. Jitsukawa, K. Kaneda, *Chem. Commun.* **2009**, 5302–5304.

[28] P. Scherrer, *Nachr. Ges. Wiss. Göttingen* **1918**, 98–100.

[29] S. Strobel, K. J. Harry, H. Duan, J. K. W. Yang, V. R. Manfrinato, K. K. Berggren, *Nanotechnology* **2011**, *22*, 375301.

[30] Y. H. Ikuhara, T. Saito, S. Takahashi, Y. Sasaki, T. Hirayama, *J. Am. Ceram. Soc.* **2012**, *95*, 524–529.

[31] S. J. Pennycook, P. D. Nellist, *Scanning Transmission Electron Microscopy: Imaging and Analysis*, Springer, Berlin **2011**.

[32] a) H. Song, R. M. Rioux, J. D. Hoefelmeyer, R. Komor, K. Niesz, M. Grass, P. Yang, G. A. Somorjai, *J. Am. Chem. Soc.* **2006**, *128*, 3027–3037; b) J. Sun, D. Ma, H. Zhang, X. Liu, X. Han, X. Bao, G. Weinberg, N. Pfänder, D. Su, *J. Am. Chem. Soc.* **2006**, *128*, 15756–15764.

[33] a) M. Pumera, J. Wang, E. Grushka, R. Polsky, *Anal. Chem.* **2001**, *73*, 5625–5628; b) Q. Cao, Y. Xu, F. Liu, F. Svec, J. M. J. Fréchet, *Anal. Chem.* **2010**, *82*, 7416–7421; c) A. Sachse, A. Galarneau, B. Coq, F. Fajula, *New J. Chem.* **2011**, *35*, 259–264.

[34] a) K. Takeda, *Rev. Sci. Instrum.* **2007**, *78*, 033103; b) K. Takeda, *J. Magn. Reson.* **2008**, *192*, 218–229.